

# Journal of Geophysical Research: Solid Earth

## RESEARCH ARTICLE

10.1029/2018JB015873

### Key Points:

- Depth-varying azimuthal and radial anisotropies are revealed in the crust and upper mantle beneath Southern California
- Possible circular asthenospheric flow is centered in the Isabella anomaly and lithospheric delamination in its surrounding areas
- Decompression melting is induced by lithospheric stretching beneath the Salton Trough

### Supporting Information:

- Supporting Information S1
- Table S1
- Table S2
- Table S3

### Correspondence to:

Y. Yu,  
yuyouqiang@tongji.edu.cn

### Citation:

Yu, Y., & Zhao, D. (2018). Lithospheric deformation and asthenospheric flow associated with the Isabella anomaly in Southern California. *Journal of Geophysical Research: Solid Earth*, 123, 8842–8857. <https://doi.org/10.1029/2018JB015873>

Received 31 MAR 2018

Accepted 28 SEP 2018

Accepted article online 1 OCT 2018

Published online 13 OCT 2018

## Lithospheric Deformation and Asthenospheric Flow Associated With the Isabella Anomaly in Southern California

Youqiang Yu<sup>1</sup>  and Dapeng Zhao<sup>2</sup> 

<sup>1</sup>State Key Laboratory of Marine Geology, Tongji University, Shanghai, China, <sup>2</sup>Department of Geophysics, Tohoku University, Sendai, Japan

**Abstract** Both laboratory experiments and seismic observations indicate that the solid Earth is composed of strongly anisotropic materials and its dynamics can be better constrained by exploring seismic anisotropy. Due to the limited number and poor depth resolution of currently available seismic anisotropy measurements, tectonic regimes of upper mantle deformations beneath Southern California still remain enigmatic and controversial. Here we present high-resolution three-dimensional models of *P* wave azimuthal and radial anisotropy in the crust and upper mantle beneath Southern California obtained by a joint inversion of local-seismic and teleseismic *P* wave data. Our results reveal significant depth-dependent anisotropy in which fast orientations in the lithospheric mantle closely follow the strike of the San Andreas fault and those in the asthenosphere are characterized as a predominantly circular pattern centered in the robust high-velocity Isabella anomaly beneath the Great Valley. The Isabella anomaly is possibly a remnant of the fossil Farallon slab and is currently experiencing a tectonic regime of lithospheric downwelling, contributing to the development of a circular asthenospheric flow. High-velocity anomalies are revealed below 300-km depth beneath areas surrounding the Great Valley, which may reflect the delaminated lithospheric segments. Different rifting processes may take place beneath the Inner Borderland and the Salton Trough whose developments are possibly related to regional mantle upwelling and lithospheric stretching, respectively.

## 1. Introduction

With the purpose of better understanding how regional tectonic units along the plate boundary deform, Southern California becomes an ideal locale to investigate complex interactions of the crust, lithospheric mantle, and asthenosphere in response to the relative motion between the Pacific and North American plates (Figure 1). Situated at the seismically most active region of southwestern United States, Southern California is bisected by the dramatic right-lateral strike-slip San Andreas fault (SAF). The SAF has developed to accommodate about 75% of the ~50 mm/year relative motion between the Pacific and North American plates, whereas the remaining 25% deformations are mostly assimilated in the Eastern California Shear Zone (Argus et al., 2011; Molnar & Dayem, 2010). The SAF was initiated by the subduction of the East Pacific Rise beneath North America, and the east-northeastward subduction of the Farallon plate was terminated at ~30 Ma by the northward migrating Mendocino triple junction (Atwater, 1970). Some fragments of the Farallon plate were incorporated into the Pacific plate such as the Monterey microplate near the western side of the Great Valley (GV; Cox et al., 2016; Jiang et al., 2018; Nicholson et al., 1994; Wang et al., 2013). Consequently, since then, deformation beneath Southern California has changed from compression to transpression, especially within the plate interface. Regional tectonic features have also developed in the Neogene that the Transverse Ranges captured by the Pacific plate experienced more than 90° clockwise rotation to its current position and extensional tectonics take place beneath the Salton Trough (Nicholson et al., 1994). These past and current tectonic deformations can be characterized and discriminated by exploring the patterns of seismic anisotropy that they would generate (Silver & Chan, 1991).

Seismic anisotropy provides an effective tool to construct the bridge for understanding the past and present deformations within the upper mantle and is usually induced by the lattice preferred orientation of anisotropic minerals such as olivine (Savage, 1999; Silver & Chan, 1991; Zhang & Karato, 1995). To detect the upper mantle anisotropy, analyzing shear wave splitting (SWS) of the core-refracted phases (PKS, SKKS, and SKS) is a very popular technique, but it is unable to discriminate the depth of the anisotropic source, and the

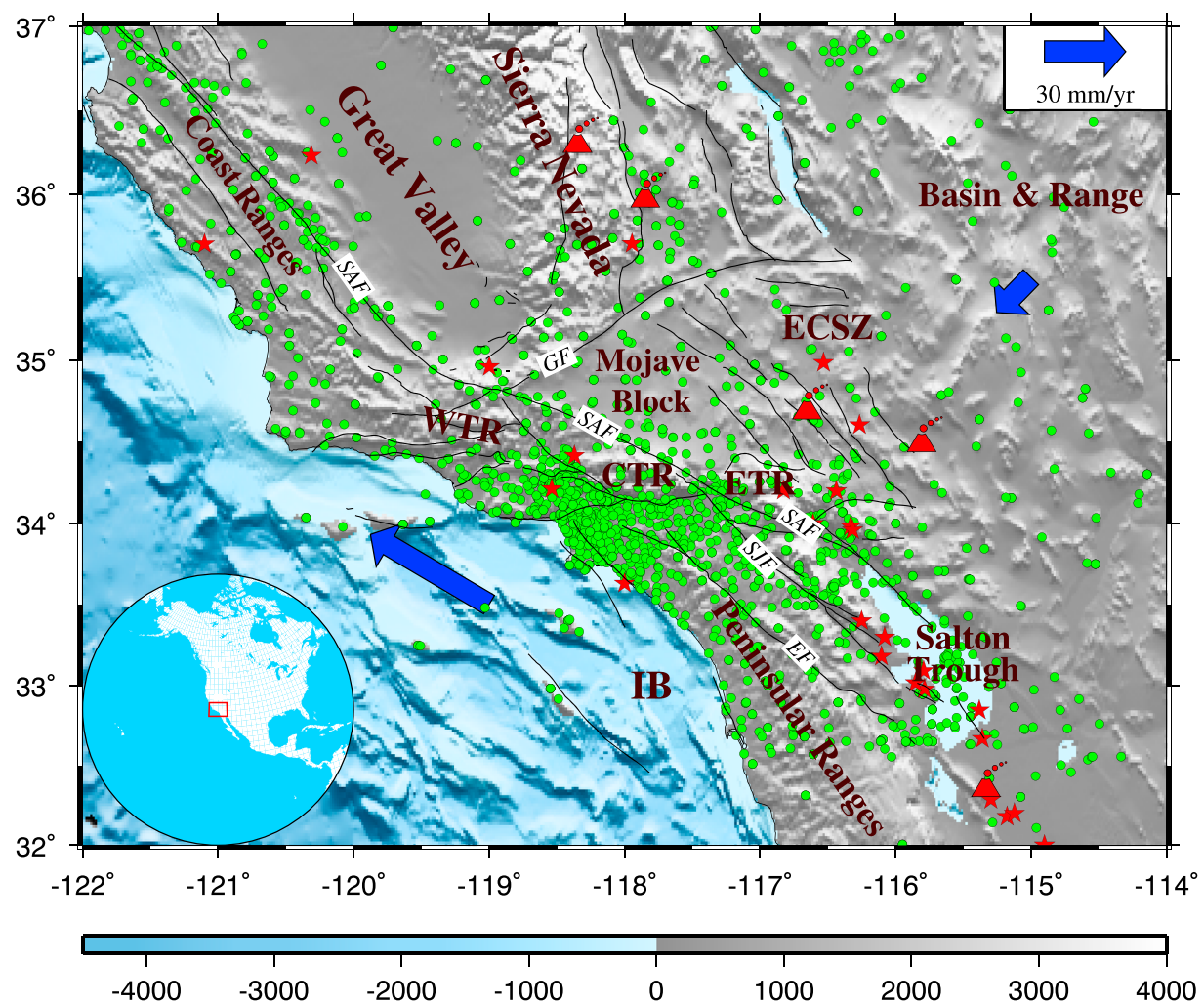


**Figure 1.** Major tectonic setting and distribution of seismic stations (green dots) used in this study. Black lines display the major faults. Red triangles are Cenozoic volcanoes. Red stars denote large earthquakes ( $M > 6.0$ ) that occurred from 1933 to 2017. Blue arrows display the absolute plate motion direction based on the NNR-MORVEL56 model (Argus et al., 2011). CTR = Central Transverse Range; ECSZ = Eastern California Shear Zone; EF = Elsinore fault; ETR = Eastern Transverse Range; GF = Garlock fault; IB = Inner Borderland; SAF = San Andreas fault; SJF = San Juan fault; WTR = Western Transverse Range. The inset map shows the location of the study area highlighted by the red rectangle.

observed splitting time is an integral effect of anisotropy from the core-mantle boundary to the surface along the raypath (Savage, 1999). Seismic anisotropy can be also revealed by surface wave studies, but the results are sometimes inconsistent with those from SWS measurements (Marone & Romanowicz, 2007; Montagner et al., 2000). The lithosphere and asthenosphere beneath Southern California were proposed to be coupled based on the observed systematic E-W fast orientations in the upper mantle from the analysis of Rayleigh waves (Yang & Forsyth, 2006) and the inversion of 5,954 SKS splitting data (Lin et al., 2014). Another earlier investigation of 3,400 SKS splitting measurements indicated that there was a poor correlation between the shallow and deep deformations (Monteiller & Chevrot, 2011). In addition, two-layer complex anisotropies were revealed from a series of SWS studies (e.g., Savage & Silver, 1993; Özalaybey & Savage, 1995; Hartog & Schwartz, 2001) in which the upper layer was closely related to lithospheric deformation, whereas the dominant E-W fast orientations were attributed to asthenospheric flow associated with the Farallon plate subduction (Liu et al., 1995; Özalaybey & Savage, 1995; Silver & Holt, 2002), toroidal flow around the edge of the sinking Gorda-Juan de Fuca slab (Zandt & Humphreys, 2008), or the shearing induced by the absolute plate motion (APM) of the North American lithosphere (Bonnin et al., 2010; Hartog & Schwartz, 2001; Kosarian et al., 2011). Small-scale mantle convections and

lithospheric delamination were proposed based on results of isotropic tomography (Humphreys & Hager, 1990; Jones et al., 2014; Schmandt & Humphreys, 2010; Zhao et al., 1996), whereas their connections with the observed seismic anisotropy were rarely discussed, which is possibly due to the fact that the results of isotropic tomography can only characterize present and static velocity structures. Thus, although extensive investigations have been conducted for Southern California, its dynamic regimes of the lithospheric deformation and mantle flow still remain poorly constrained.

In this study, we aim to simultaneously determine high-resolution three-dimensional (3-D) isotropic and anisotropic velocity images of the crust and upper mantle beneath Southern California by applying advanced anisotropic tomography techniques to both local-seismic and teleseismic  $P$  wave data (Wang & Zhao, 2008, 2013). Our results reveal significant depth-dependent anisotropy and shed new light on the lithospheric deformation and mantle dynamics beneath Southern California. In our study area, the common A-type olivine fabrics are expected to dominantly exist in the upper mantle (Barak & Klemperer, 2016).  $P$  wave azimuthal anisotropy obtained from our tomographic inversion is similar to those from the SWS measurements that mainly reveal the anisotropic orientations in the horizontal plane. In contrast, radial anisotropy works as a proxy for plastic flow directions within the upper mantle in the vertical plane, and positive and negative radial anisotropies indicate horizontal and vertical flows, respectively (Wang & Zhao, 2013).

## 2. Data and Methods

### 2.1. Data Selection and Analysis

The seismic data used in this study were recorded at a total of 1,673 stations (Figure 1) and from two databases. Arrival times of local earthquakes during 1949 to 2017 were requested from the Southern California Earthquake Data Center (<http://scedc.caltech.edu>). The travel time data of teleseismic events during 1965 to 2014 with epicentral distances ranging from  $30^\circ$  to  $90^\circ$  were downloaded from the International Seismological Centre (ISC; <http://www.isc.ac.uk>) and had been manually reviewed by the ISC staff. The picking accuracy is 0.1 s or better for most of the data (Tian et al., 2007). Events recorded at less than 10 seismic stations are removed. To get a more uniform distribution of earthquakes than those in the original catalog, we divided the study area into cells with lateral and vertical intervals of 8 and 2 km, respectively, which are set as  $0.1^\circ$  and 10.0 km for areas outside of Southern California. In each cell, we select only one event following a criterion that the event was recorded by the maximum number of stations.

Most of the travel time residuals for both the selected local and teleseismic events fall in the range of  $\pm 1.0$  s (Figure 2). In order to minimize the effects of hypocentral mislocations, we use both  $P$  and  $S$  wave arrivals to relocate all the local earthquakes. The relocated events with uncertainties  $<4$  km in focal depth,  $<0.04^\circ$  in epicentral location, and  $<0.4$  s in origin time are used to conduct the tomographic inversions. As a result, our final data set contains 579,072  $P$  wave arrivals from 16,600 local earthquakes and 280,441  $P$  wave arrivals from 12,491 teleseismic events (Figure 3). Theoretical travel times are calculated for the IASP91 Earth model with the Moho topography (Tape et al., 2012; Figure S1) taken into account. Most parts of the study area are well covered by the crisscrossing rays, especially beneath the coastal and continental regions (Figure 4).

### 2.2. Isotropic and Anisotropic Tomography

We investigate the 3-D velocity structure beneath the study area using the isotropic tomography method of Zhao et al. (1992, 1994), which can deal with lateral depth variations of seismic discontinuities (e.g., the Moho) in the study region. Here we only briefly introduce the methods of radial and azimuthal anisotropy tomography (Wang & Zhao, 2008, 2013). The anisotropy is commonly considered to possess an axis of hexagonal symmetry, which is quite close to the realistic Earth model and greatly reduces unknown parameters for tomographic inversion (e.g., Huang & Zhao, 2013; Maupin & Park, 2007; Wang & Zhao, 2008). Under the assumption of weak azimuthal anisotropy with a hexagonal symmetry axis in the horizontal direction, we can approximately express the  $P$  wave slowness as the following (Backus, 1965; Wang & Zhao, 2008):

$$S(\varphi) = S_0[1 + A \cos(2\varphi) + B \sin(2\varphi)], \quad (1)$$

where  $S$  and  $S_0$  indicate the total slowness and azimuthal average slowness (i.e., the isotropic component), respectively.  $A$  and  $B$  represent two azimuthal anisotropy parameters, and  $\varphi$  is the raypath azimuth. The fast orientation ( $\psi$ ) and the amplitude ( $\alpha$ ) of azimuthal anisotropy can be expressed as

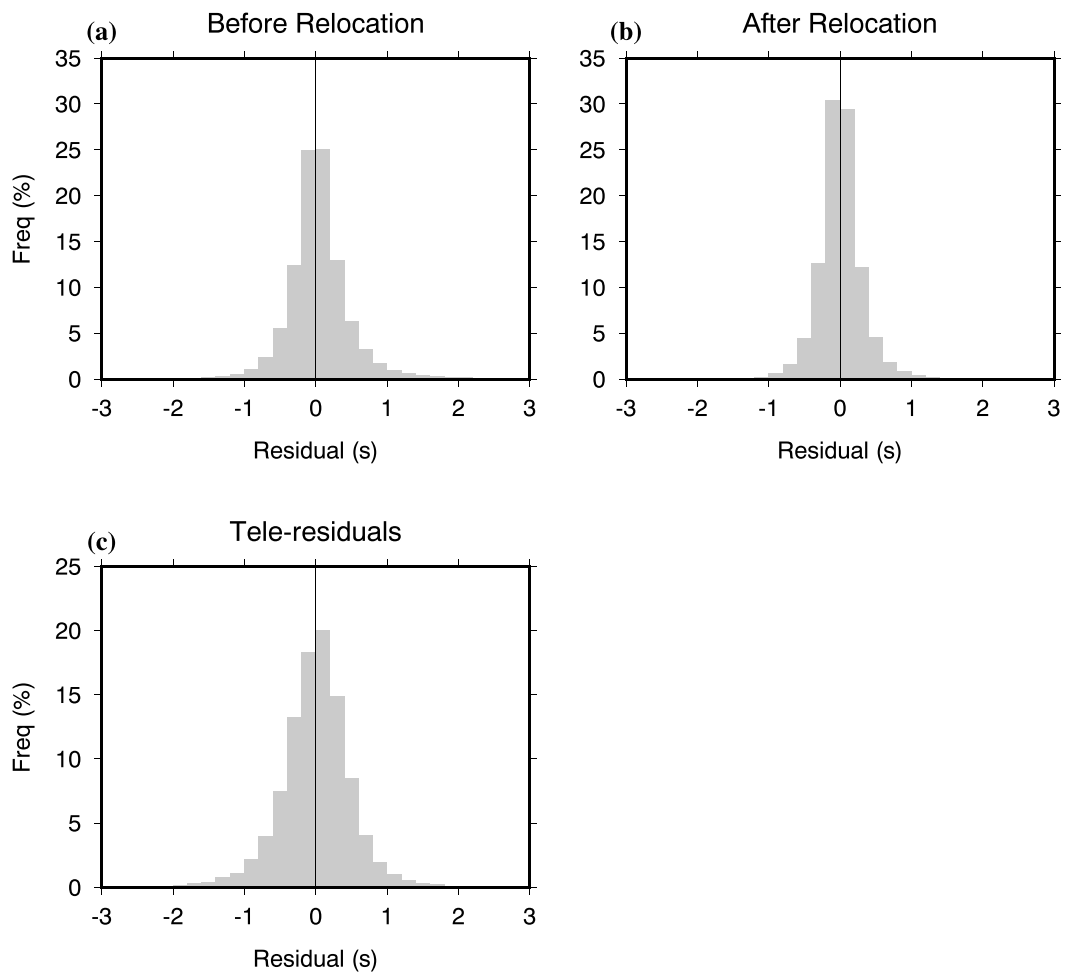


**Figure 2.** Histograms of  $P$  wave travel time residuals. Local earthquake travel time residuals (a) before and (b) after the earthquake relocation. (c) Relative travel time residuals of teleseismic events.

$$\psi = \begin{cases} \frac{1}{2} \tan^{-1} \left( \frac{B}{A} \right) + \begin{cases} \frac{\pi}{2}, & A > 0 \\ 0, & A < 0 \end{cases} \\ -\frac{\pi}{4}, & A = 0, B > 0 \\ \frac{\pi}{4}, & A = 0, B < 0 \end{cases} \quad (2)$$

$$\alpha = \frac{V_f - V_s}{2V_0} = \frac{\sqrt{A^2 + B^2}}{1 - (A^2 + B^2)} \quad (3)$$

where  $V_0$  is the isotropic velocity, and  $V_f$  and  $V_s$  correspond to velocities in the fast and slow orientations, respectively (Wang & Zhao, 2008).

Radial anisotropy is characterized as revealing the difference between the horizontal and vertical velocities and usually assumed to have a vertical axis of hexagonal symmetry. Under such an assumption, equation (1) can be rewritten as (Wang & Zhao, 2013)

$$S = S_0 [1 + C \cos(2\theta)] \quad (4)$$

where  $C$  is the parameter for radial anisotropy and  $\theta$  is the incident angle of a raypath. The amplitude ( $\beta$ ) of the radial anisotropy is expressed as

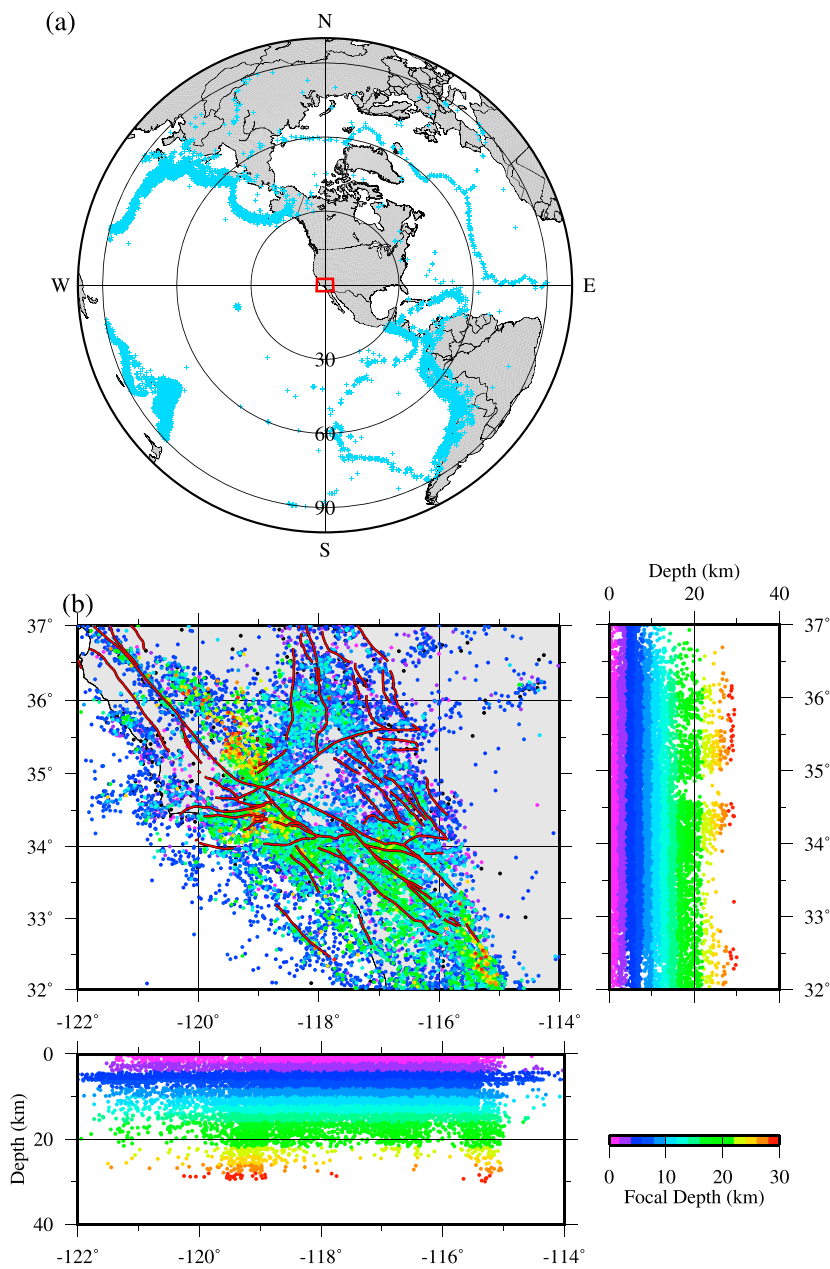


**Figure 3.** Distributions of 12,491 teleseismic events (a) and 16,600 local earthquakes (b) used in this study. The red lines denote active faults in the study region. Colors of the dots denote the focal depths.

$$\beta = \frac{Vp_h - Vp_v}{2V_0} = \frac{C}{1 - C^2} \quad (5)$$

where  $Vp_h$  and  $Vp_v$  are  $P$  wave velocities in the horizontal and vertical directions, respectively. Thus, positive  $\beta$  means a faster  $P$  wave velocity in the horizontal direction ( $Vp_h/Vp_v > 1$ ), and vice versa.

Tomographic inversions for 3-D isotropic velocity, 3-D radial anisotropy, and 3-D azimuthal anisotropy are individually conducted. One set of 3-D grid is set up to invert for the 3-D isotropic velocity model. However, two sets of 3-D grid are adopted for models of the radial and azimuthal anisotropy tomography. One fine grid is used to express the 3-D isotropic velocity, whereas the other coarse grid is used to express the anisotropic structure, because better azimuthal coverage of rays is required for determining the anisotropic parameters (Huang & Zhao, 2013; Wang & Zhao, 2008). The iterative conjugate-gradient LSQR algorithm

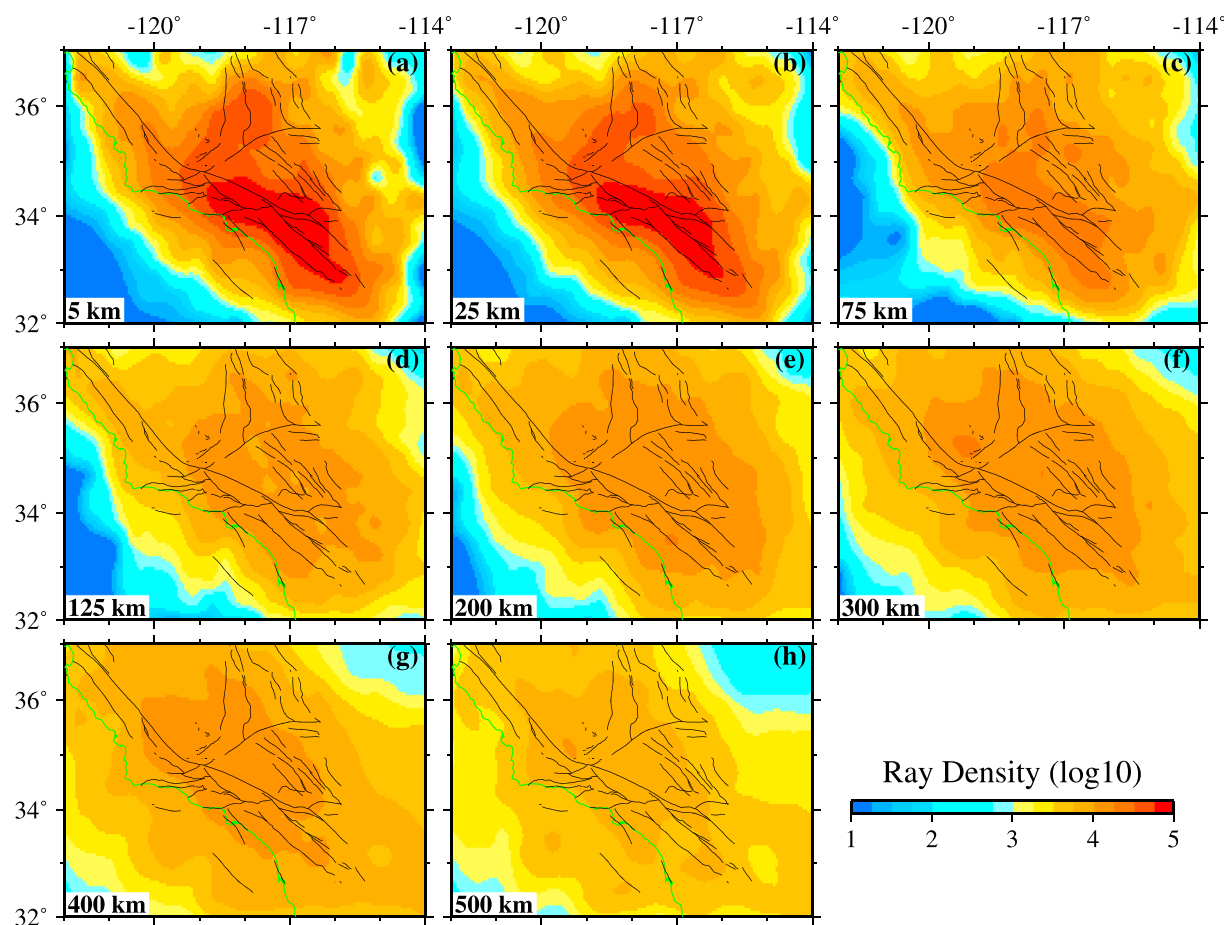


**Figure 4.** Density distribution of  $P$  wave rays at different depths. The green line denotes the coastal line. The black lines indicate active faults.

with damping and smoothing regularizations is employed to solve the large and sparse system of observation equations (Zhao et al., 1992, 1994). The optimal damping and smoothing parameters are determined based on the trade-off curves between the root-mean-square travel time residual and norm of the solution (Figure S2 in the supporting information). The smoothing parameter is firstly determined with an initial damping value of 80, and the optimal smoothing value is found to be 0.001, which is then used for determining the damping parameter (Figure S2). As a result, the optimal damping parameter is found to be 100 (Figure S2). Given the decent azimuthal coverage of the events (Figure 3) and the dense seismic network (Figure 1), the trade-off between seismic anisotropy and heterogeneity is considered to be insignificant (Huang et al., 2015). Extensive checkerboard resolution tests are conducted (Figures S3–S15), and the test results show that the isotropic and anisotropic tomographic models have a lateral resolution of  $0.3^\circ$  and  $0.6^\circ$ , respectively. Hence, we adopt the horizontal grid intervals of  $0.3^\circ$  and  $0.6^\circ$  for inverting for the final velocity and anisotropy parameters, respectively. Meshes of grid nodes are arranged at depths of 5, 25, 75, 125, 200, 300, 400, and 500 km in the crust and upper mantle. To evaluate the robustness of main features of the tomographic images, we have also performed restoring resolution tests with input models derived from the tomographic results (Figures S16–S21). Gaussian noise with a standard deviation of 0.1 s is added to the theoretical travel times in all the synthetic tests. The final 3-D models of  $P$  wave velocity relative to the IASP91 Earth model, and azimuthal and radial anisotropies relative to the 3-D velocity model are shown in Tables S1–S3, respectively.

### 2.3. Two-Layer Fitting of SWS Measurements

A model of two anisotropic layers is usually adopted to investigate complex anisotropy characterized as azimuthal variations of the SWS measurements with approximately  $\pi/2$  periodicity (Silver & Savage, 1994). In this

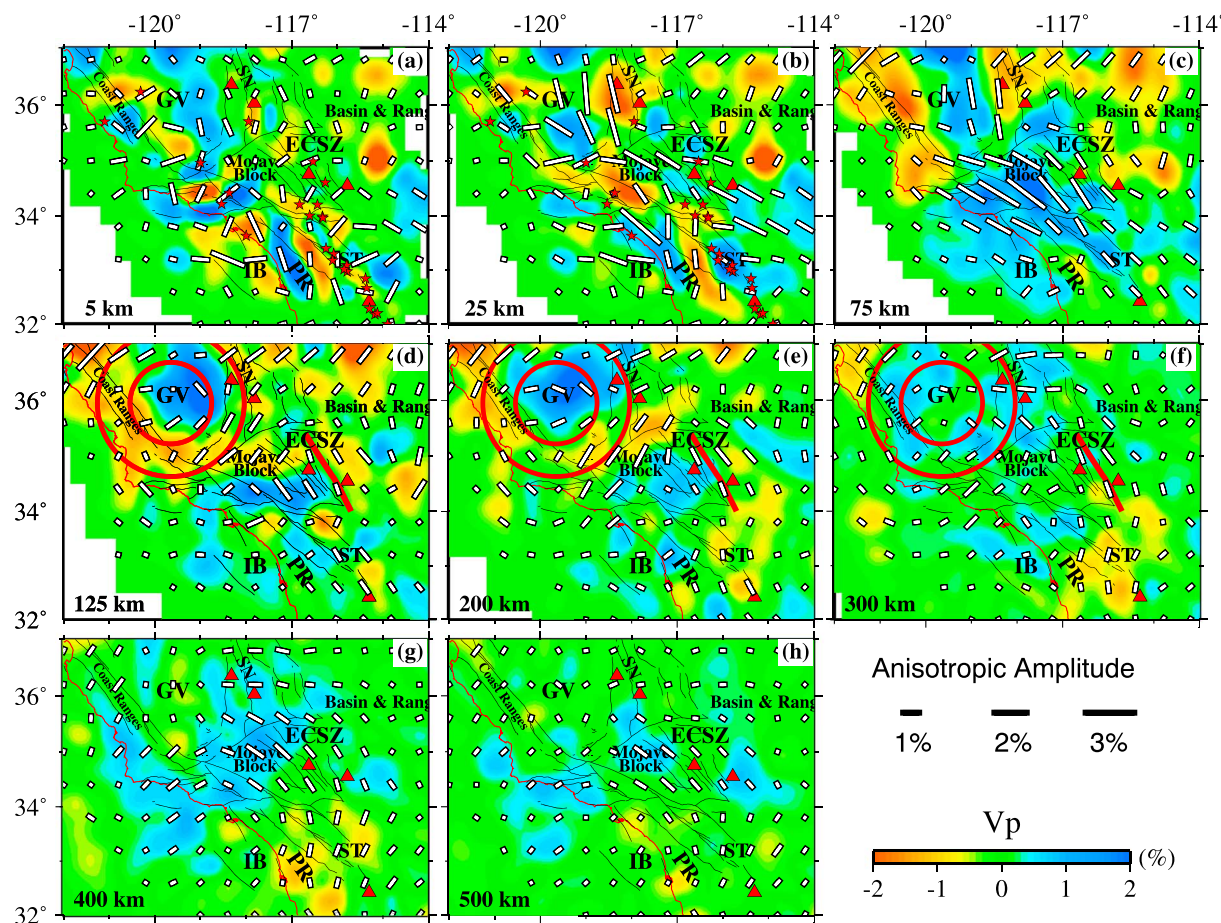


**Figure 5.** Map views of  $P$  wave isotropic tomography and azimuthal anisotropy. The orientation and length of the white bars denote the fast-velocity direction and the amplitude of azimuthal anisotropy, respectively. The background colors show  $P$  wave velocity variations from isotropic tomography. The red circles and the red thick line in (d)–(f) typically depict the circular pattern of azimuthal anisotropy and deflected mantle flow, respectively. GV = Great Valley; PR = Peninsular Ranges; SN = Sierra Nevada; ST = Salton Trough; ECSZ = Eastern California Shear Zone; IB = Inner Borderland. The other symbols are the same as those in Figure 1.

study, we employ a misfit function to determine the optimal anisotropic parameters of the two layers beneath Southern California by grid searching of fast orientations and splitting times in the range of  $0^{\circ}$ – $180^{\circ}$  and  $0.5$ – $2.0$  s, respectively (Gao & Liu, 2009; Silver & Savage, 1994). The misfit function is expressed as

$$\epsilon^2 = \sum_{i=1}^n w_1 \times \left[ \frac{(\psi_i^{\text{obs}} - \psi_i^{\text{cal}})}{\sigma_{\psi_i}} \right]^2 + w_2 \times \left[ \frac{(\delta t_i^{\text{obs}} - \delta t_i^{\text{cal}})}{\sigma_{\delta t_i}} \right]^2 \quad (6)$$

where  $(\psi_i^{\text{obs}}, \delta t_i^{\text{obs}})$  and  $(\psi_i^{\text{cal}}, \delta t_i^{\text{cal}})$  are the observed and calculated pairs of fast orientation and splitting time of the  $i$ th measurement, respectively,  $n$  is the number of measurements,  $\sigma_{\psi_i}$  and  $\sigma_{\delta t_i}$  are the standard deviations of the  $i$ th  $\psi$  and  $\delta t$ , respectively, and  $w_1$  and  $w_2$  are the weighting factors with a sum equal to 1, which are set as 0.8 and 0.2, respectively. The fitting accuracy is estimated to be  $\pm 25^{\circ}$  in  $\psi$  and  $\pm 0.3$  s in  $\delta t$  (Savage & Silver, 1993).

### 3. Results and Discussion

As a whole, the resulting isotropic 3-D  $V_p$  model (Figures 5 and S16) is consistent with those of previous tomographic studies (e.g., Boyd et al., 2004; Humphreys et al., 1984; Humphreys & Hager, 1990; Jiang et al., 2018; Raikes, 1980; Schmandt & Humphreys, 2010; Tape et al., 2009; Tian et al., 2007; Zhao et al., 1996). In the crust, sedimentary basins are well imaged as low-velocity (low- $V$ ) anomalies. The batholith

of the Mesozoic Peninsula Ranges is divided into western and eastern portions based on the observed high- and low-velocity anomalies, respectively, which is possibly due to the development of more mafic crust beneath the western terrane (Lewis et al., 2000). Prominent lithospheric roots are revealed as high-velocity (high-V) anomalies beneath batholiths such as the GV, the Transverse Ranges, the Mojave Block, and the Peninsula Ranges. Accordingly, low-V anomalies are revealed in the lithospheric mantle beneath some weak areas like the Inner Borderland, the Salton Trough, the Coast Range, and the Sierra Nevada. In contrast, substantial high-V anomalies exist at depths of ~300 to 500 km beneath the central SAF and areas surrounding the GV, which are also revealed by previous tomographic studies (Schmandt & Humphreys, 2010; Sigloch et al., 2008).

### 3.1. Depth-Dependent Azimuthal Anisotropy

Azimuthal anisotropies in the lower crust and lithospheric mantle beneath areas adjacent to the SAF are poorly correlated (Figures 5b and 5c), possibly indicating their decoupling tectonic regime (Hartog & Schwartz, 2001), which is consistent with results from a joint inversion of ambient noise and earthquake data in the western United States (Lin et al., 2011). Geodetic evidence indicates that the viscosity of the lower crust is relatively high (Meade & Hager, 2005) and nonbrittle deformation dominantly develops to accommodate the right-lateral shear in the lower crust (Hartog & Schwartz, 2001). Crustal anisotropy is usually associated with shape-preferred orientation, and the observed complex patterns can be attributed to fossilized fabric within schists in the lower crust (Porter et al., 2011), regional stresses, active faults, local tectonic features, and rock types (Li & Peng, 2017). In comparison, azimuthal anisotropy in the lithospheric mantle systematically follows the strike of the SAF (Figure 5) where the magnitude of anisotropy is dependent on the strain rates and decreases with the distance from the SAF. The relative plate motions between the Pacific and North American plates possibly place significant shear forces along the SAF, which align the anisotropic minerals within the lithospheric mantle and develop the observed fault-parallel azimuthal anisotropy (Hartog & Schwartz, 2001; Savage, 1999). Thus, the SAF may be a large-scale lithospheric feature and penetrate into the mantle (Tanimoto & Prindle Sheldrake, 2002).

A circular pattern of the fast orientations is highlighted in the upper asthenosphere (Figures 5d and 5e) and centered in the GV where its lithosphere (Figures 5a–5c) is characterized as possessing coherent N-S fast orientations. To quantify the matching between the resulting fast orientations and the circular trend, we calculated their absolute angle differences (Figure 6), which are mostly less than 30° for the majority of the areas surrounding the GV. The matching results beneath the Sierra Nevada (Figure 6) become worse at greater depths, which are possibly influenced by other factors such as the APM and deep mantle perturbations. Such a circular asthenospheric anisotropy is totally different from the fault-parallel anisotropy in the lithospheric mantle, suggesting the existence of complex anisotropy in the upper mantle, which is also supported by SWS measurements (Figure 7). Considering the quantity and location of the SWS measurements and features of the resulting azimuthal anisotropy, we explored the complex anisotropy beneath part of the central SAF (Figure 7), which has been extensively studied during the last two decades (e.g., Bonnin et al., 2010; Hartog & Schwartz, 2001; Özalaybey & Savage, 1995; Polet & Kanamori, 2002; Savage & Silver, 1993; Silver & Savage, 1994). A two-layer model is usually employed to explore complex anisotropy based on the SWS measurements (Silver & Savage, 1994). Our two-layer fitting of the SWS measurements well determines the optimal model that the upper layer (the lithosphere) has a fault-parallel fast orientation of 142° and the lower layer (the asthenosphere) owns a fast orientation of 69° consistent with the circular pattern. The resulting parameters characterizing the complex anisotropy are also consistent with results of the previous SWS studies (e.g., Bonnin et al., 2010; Hartog & Schwartz, 2001; Özalaybey & Savage, 1995). Therefore, the lithosphere and asthenosphere beneath the SAF are significantly decoupled, and their anisotropies are possibly induced by different tectonic regimes.

NE-SW fast orientations are coherently revealed in the lithosphere and asthenosphere beneath the Basin and Range at the NE corner of our study region (Figure 5), closely consistent with the APM of the North American plate and the SWS measurements (Figures 1 and 7). Southwestward dragging from the North American plate motion may induce significant shearing and viscous coupling deformation between the lithosphere and the asthenosphere, leading to the resulting APM-parallel fast orientations. Compilation of the SWS database for the western and central United States (Yang et al., 2016) also indicates that the APM plays a significant role in generating azimuthal anisotropy with the NE-SW fast orientations.

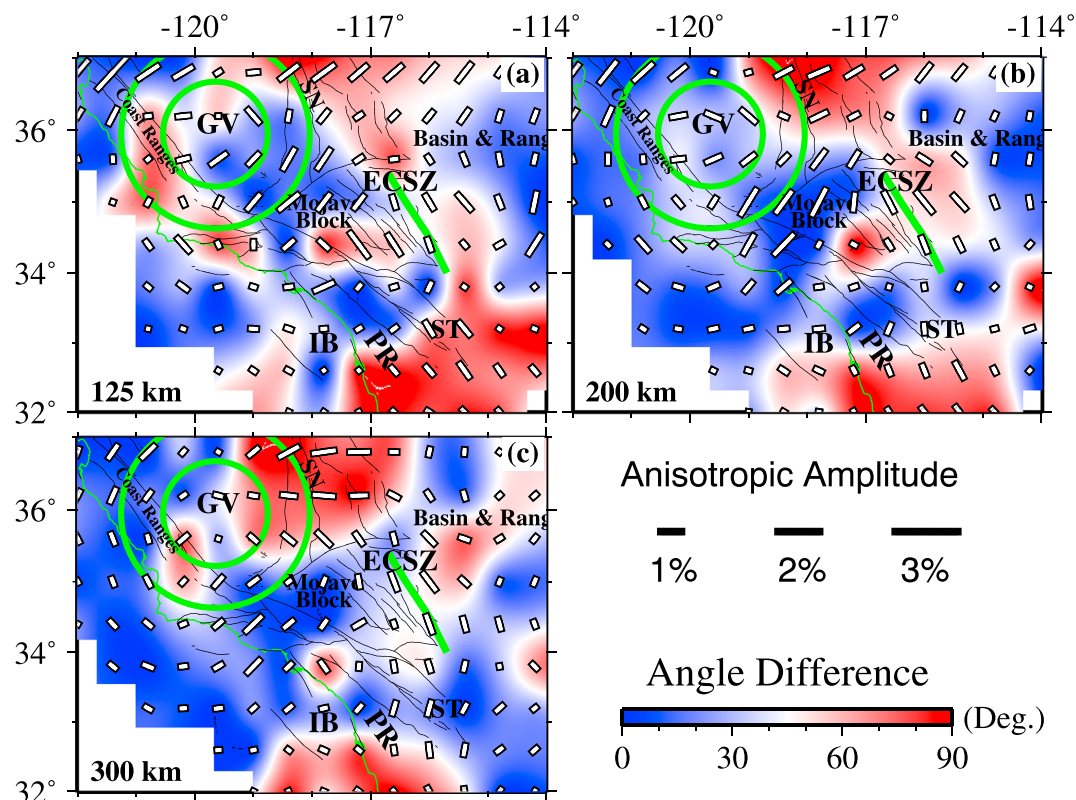


**Figure 6.** The colors denote the absolute angle differences between the resulting fast  $V_p$  orientations at depths of 125, 200, and 300 km and the trend of the proposed circles centered in the Great Valley. The absolute angle differences at each point are calculated by subtracting the fast  $V_p$  orientations from the tangent angle of the circle that is centered in the Great Valley, and its radius is the distance between each point and the center of the Great Valley. The color scale is shown at the bottom. The other symbols are the same as those in Figure 5. ECSZ = Eastern California Shear Zone; GV = Great Valley; PR = Peninsular Ranges; SN = Sierra Nevada; ST = Salton Trough; IB = Inner Borderland.

### 3.2. Lithospheric Downwelling and Asthenospheric Flow

A prominent high- $V$  anomaly existing beneath the GV, known as Isabella anomaly (Raikes, 1980), extends from near the base of the crust into the asthenosphere (Figures 5 and 8), which has been imaged by many previous studies (Gilbert et al., 2012; Humphreys & Hager, 1990; Jones et al., 2014; Raikes, 1980; Schmandt & Humphreys, 2010; Tanimoto & Prindle Sheldrake, 2002; Tian et al., 2007; Zhao et al., 1996). Various origins of the Isabella anomaly have been proposed, which is interpreted as a remnant of the subducted Farallon slab (Bird & Rosenstock, 1984; Cox et al., 2016; Jiang et al., 2018; Raikes, 1980; Wang et al., 2013; Zhao et al., 1996) or lithospheric pieces associated with delamination or convective removal of dense materials from beneath the Sierra Nevada (Boyd et al., 2004; Gilbert et al., 2012; Jones et al., 2014; Zandt et al., 2004). Our results show that the Isabella anomaly exhibits an overwhelming negative radial anisotropy (Figure 8), possibly indicating a downwelling motion, and systematical N-S fast orientations in the lithosphere that are seriously oblique to the APM of the North American plate. Similar features are also observed beneath central Tibet (Zhang et al., 2016) and central Wyoming (Li et al., 2017) where the downwelling lithospheres are clearly imaged as high- $V$  anomalies with negative radial anisotropy. The relatively high viscosity of the high- $V$  mantle blocks possibly plays a dominant role in the characterization of mantle downwelling as negative radial anisotropy (Li et al., 2017). Assuming that the Isabella anomaly is generated by convective removal of lithospheric materials from the southern Sierra Nevada, one may expect to observe generally E-W fast orientations in the lithosphere, which is not consistent with our results (Figure 5). Such a mechanism is also difficult to explain the robust high- $V$  anomalies around 300-km depth beneath areas surrounding the Isabella anomaly. In addition, the position of the Isabella anomaly in the mantle fails to support the connection between the Isabella anomaly and the Sierra

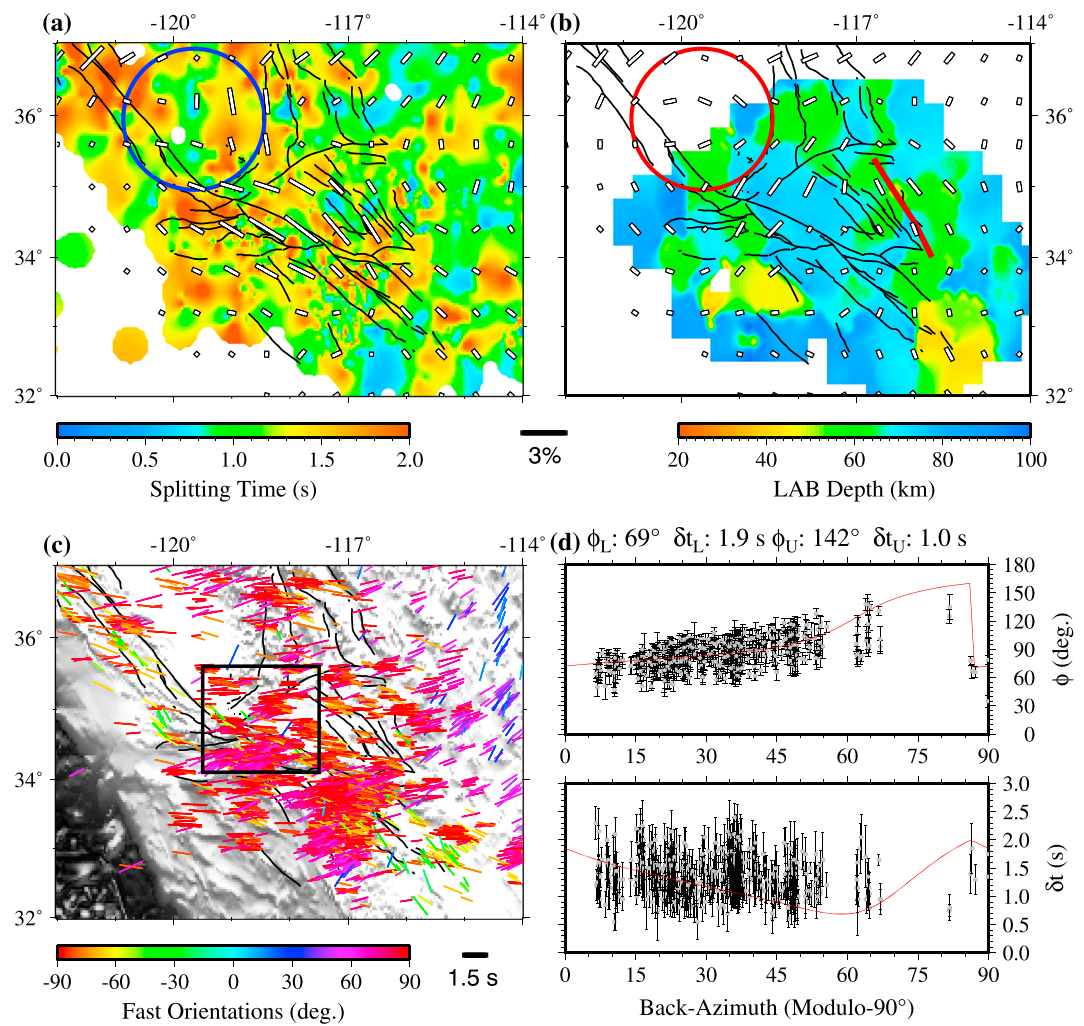


**Figure 7.** (a) Comparison of fast velocity directions (white bars) of  $P$  wave azimuthal anisotropy at 75-km depth determined by this study with the distribution of delay times (colors) of shear wave splitting (SWS) measurements (Barak & Klemperer, 2016; Ramsay et al., 2016; Yang et al., 2016). (b) Comparison of the lithospheric thickness (white bars) at 200-km depth determined by this study with  $P$  wave azimuthal anisotropy (white bars) at 200-km depth determined by this study. (c) Distribution of the SWS measurements. The color and length of each bar denote the fast polarization direction and the SWS delay time, respectively, whose scales are shown below (c). Observations within the black rectangles are used in Figure 7d. (d) Two-layer fitting of the SWS measurements. The upper and lower panels show the results for the fast polarization direction and the delay time, respectively. The red lines show the modeling results, whereas the vertical bars denote the observed values (open circles) and their standard deviations. ( $\phi_U, \delta t_U$ ) and ( $\phi_L, \delta t_L$ ) are the optimal values of the fast orientation and splitting time for the upper and lower layers, respectively.

Nevada (Jiang et al., 2018). Thus, we favor the interpretation that the Isabella anomaly is instead a fossil slab fragment of the Farallon plate (Cox et al., 2016; Jiang et al., 2018; Nicholson et al., 1994; Wang et al., 2013). The resulting N-S fast orientations in the lithosphere of the GV possibly represent fossil anisotropy inherited from the subducted Farallon plate where trench-parallel fast orientations are expected to develop, which has been extensively observed in the subducting slabs surrounding the Pacific (e.g., Liu & Zhao, 2017; Long & Silver, 2008; Wei et al., 2016; Zhao et al., 2016). The observed trench-parallel fast orientations within the slab are more likely to be induced by frozen-in anisotropy formed at the mid-ocean ridge or the lattice-preferred orientation of the B-type olivine (Wang & Zhao, 2013).

The Isabella anomaly is revealed to be possibly attached to the Monterey microplate (Cox et al., 2016; Jiang et al., 2018; Nicholson et al., 1994; Wang et al., 2013). Modeling results (Pikser et al., 2012) indicate that it is feasible to transport the Isabella anomaly hundreds of kilometers along-strike to its current place

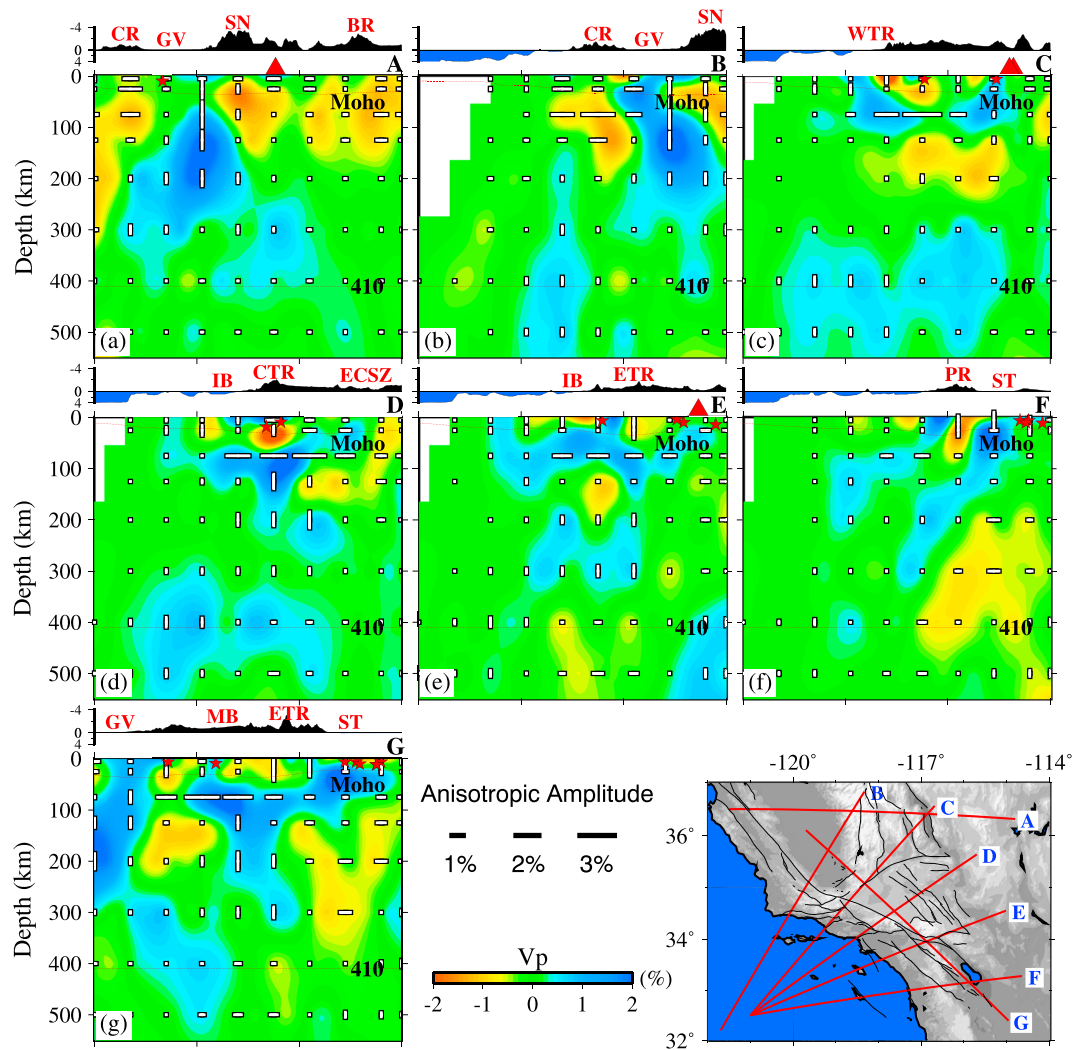


**Figure 8.** Vertical cross sections of  $P$  wave isotropic tomography and radial anisotropy. The horizontal white bars indicate that the horizontal velocity is faster than the vertical velocity and vice versa. The length of the bars denotes the amplitude of radial anisotropy. Red stars and triangles denote large earthquakes ( $M > 6.0$ ) and Cenozoic volcanoes shown in Figure 1, respectively, within a 50-km width of each profile. BR: Basin and Range; CR: Coast Ranges; MB: Mojave Block.

while remaining intact and attached. Since the cessation of the Farallon plate subduction around 30 Ma, the Isabella anomaly has been experiencing deformations of the oblique convergent motion between the Pacific and North American plates (Bird & Rosenstock, 1984). The oceanic composition of the Isabella anomaly can easily put itself in a gravitationally metastable state due to the density contrast and promote the occurrence of lithospheric downwelling. Numerical modeling of the Great Basin predicts that downwelling of the lithosphere into the asthenosphere can be activated by a density anomaly of as little as 1% (West et al., 2009). The Isabella anomaly is possibly experiencing a process of ongoing lithospheric downwelling, which can induce much more substantial modification of regional fabrics (West et al., 2009) highlighted by the resulting outstanding circular pattern of azimuthal anisotropy in the asthenosphere. Lithospheric downwelling of the Isabella anomaly can exert a downward pull to the base of the overlying crust and lead to overlying subsidence (Houseman & Molnar, 1997), which is supported by the surface topography and numerical modeling (Fay et al., 2008). The sinking of the Isabella anomaly must be much slower than the plate motion rate for it to be at its current position. Significant dropping of the Isabella anomaly may have occurred only in the past a few million years, possibly due to the change of slab geometry and the enhancement of oblique convergence at the

western Transverse Range. Clockwise rotation makes the western Transverse Range sit close to the Isabella anomaly and become the most compressional place in Southern California (Bird & Rosenstock, 1984; Nicholson et al., 1994; Raikes, 1980).

The downwelling Isabella anomaly may trigger mantle upwelling in its surrounding areas (Göğüş et al., 2017) where systematical negative radial anisotropies are revealed in the asthenosphere (Figure 8). The upwelling mantle flow is possibly twisted by the right-lateral strike-slip SAF when it approaches the transition between the lithosphere and asthenosphere, resulting in a rotated pattern of flow system in the horizontal direction consistent with the observed circular pattern of azimuthal anisotropy and systematical positive radial anisotropy (Figures 5 and 8). Such a flow system is also revealed as anomalously high heat flow (Lachenbruch & Sass, 1980) and relatively larger SWS delay times (Figure 7). The hot asthenosphere brought by the upwelling asthenospheric flow may create melting of the lower lithosphere and induce the development of lithospheric delamination, which is estimated to occur at ~3.5 Ma based on a sudden pulse of mafic magmatism at the Sierra Nevada from 4 to 3 Ma (Manley et al., 2000). The delaminated lithosphere drops down to the asthenosphere and is replaced by hot materials from the asthenospheric flow, forming the observed low-V anomalies (Boyd et al., 2004) and providing dynamic support to the ranges of the southern Sierra Nevada and the Coast Ranges (Manley et al., 2000). The high-V anomalies imaged at ~300-km depth are located exactly beneath the ranges surrounding the GV and most likely correspond to the segments of the delaminated lithosphere, which helps answer the long-lasting puzzle of where the removed lithospheric root of the southern Sierra Nevada might be at present (Jones et al., 2014). Numerical modeling investigations proposed that the growth period of delamination takes an order of magnitude shorter time (Beall et al., 2017), which is consistent with the depth distribution of high-V anomalies (Figure 5) that are much shallower beneath the GV (~200-km depth) than those beneath its surrounding ranges (~300-km depth).

Similar lithospheric delamination also occurs beneath the Mojave Block and the Transverse Ranges where the upper and lower lithospheres exhibit positive and negative radial anisotropies, respectively (Figure 8). Active melting from possibly small-scale mantle convection (Fay et al., 2008) contributes to the peeling away of dense materials from the lower lithosphere. This ongoing delamination has left footprints in the mantle transition zone where significant high-V anomalies (Figure 5) are detected (Schmandt & Humphreys, 2010; Sigloch et al., 2008), possibly corresponding to the delaminated lithospheric segments. Meanwhile, mantle flow associated with the APM or the Isabella anomaly is regionally disturbed by the topography of lithosphere and altered at the boundary of thick lithospheric root (Lekic et al., 2011) such as the Eastern California Shear Zone (Figure 7) where the flow is deflected to propagate in a NW-SE direction.

### 3.3. Rifting at the Inner Borderland and Salton Trough

In Southern California, there are predominantly two rift regions situated at the Inner Borderland and the Salton Trough where significant lithospheric thinning is revealed by receiver function investigations (Lekic et al., 2011; Reeves et al., 2015). Based on the resulting distinct features of both the azimuthal and radial anisotropies, mechanisms of rifting at the Inner Borderland and the Salton Trough possibly follow distinct modes. Previous isotropic tomography studies usually interpreted the low-V anomaly beneath the Salton Trough as mantle upwelling to accommodate for the oblique spreading (Humphreys et al., 1984; Raikes, 1980; Schmandt & Humphreys, 2010; Tian et al., 2007), which is further supported by weak anisotropy from tomographic analyses of SWS data (Monteiller & Chevrot, 2011). However, recent SWS analysis detected significant anisotropy beneath the Salton Trough with an average splitting delay time of about 1.2 s and fast orientations aligned in the NW-SE transform shear direction (Barak & Klemperer, 2016), which is well consistent with our results (Figure 7) and argues against the model of mantle upwelling.

A conspicuous high-V anomaly resting around the Moho has been revealed beneath the Salton Trough (e.g., Han et al., 2016; Hauksson, 2000; Jiang et al., 2018; Lee et al., 2014; Tape et al., 2009), whereas its asthenosphere is depicted as a comparatively low-V anomaly (e.g., Humphreys et al., 1984; Raikes, 1980; Schmandt & Humphreys, 2010). The crustal high-V anomaly possibly reflects a shallow Moho depth or the ongoing upward basaltic intrusion where negative radial anisotropy (Figure 8) and high heat flow are revealed (Lachenbruch et al., 1985; Lachenbruch & Sass, 1980). Intrusion of basaltic magma induces the emplacement of higher density igneous rocks ponding around the Moho and then forms the oceanic basement beneath the Salton Trough (Elders et al., 1972; Han et al., 2016). Evidence from seismic reflections (Brothers et al., 2009; Han et al., 2016) indicates that relative motion between the Pacific and North

American plates beneath the Salton Trough generates a transtension force, leading to lithospheric stretching and the formation of pull-apart basins (Elders et al., 1972). The decrease of lithospheric loading in turn induces decompression melting in the upper mantle imaged as a low-V anomaly (Figure 8). The vertical melt pockets in the upper mantle are aligned in the shear direction and further develop the rift-parallel azimuthal anisotropy with NW-SE fast orientations (Barak & Klemperer, 2016), which is also supported by the uniformly positive radial anisotropy (Figure 8). Rift-parallel azimuthal anisotropy induced by oriented magmatic cracks in the mantle is also observed beneath other continental rifts such as the Kenya rift (Gao et al., 1997). Thus, the Salton Trough seems to follow a passive rifting model that rifting is activated by the oblique strike-slip plate motions and the decompressed melt pocket is directed to align horizontally instead of upwelling, which is similar to the incipient Okavango rift in southern Africa where the APM plays the primary role (Yu et al., 2017).

In contrast, rifting beneath the Inner Borderland seems to follow more like an active model that mantle upwelling is currently taking place based on the prominent low-V anomalies in the asthenosphere and the significant negative radial anisotropy (Figure 8). Lithospheric thinning beneath the Inner Borderland (Lekic et al., 2011) is clearly revealed (Figure 7). Mantle flow possibly associated with small-scale mantle convections beneath the Transverse Ranges and adjacent areas (Fay et al., 2008; Schmandt & Humphreys, 2010) can be released to upwelling in places where the lithosphere becomes weak (Figure 8). The sinking of the delaminated lithospheric segments into the mantle transition zone beneath the Transverse Ranges may also contribute to mantle upwelling. The rotation of the Traverse Range possibly makes the Inner Borderland a relatively lithospheric weak zone (Nicholson et al., 1994; Reeves et al., 2015), which offers the chance for the mantle flow to migrate upward, providing the driving force for rifting beneath the Inner Borderland.

#### 4. Conclusions

The first high-resolution model of 3-D isotropic and anisotropic (including azimuthal and radial anisotropy) tomography of the crust and upper mantle beneath Southern California is determined using a large quantity of both local-seismic and tele-seismic  $P$  wave arrival-time data. Depth-varying azimuthal anisotropy is revealed around the SAF where the fast orientations change from fault-parallel in the lithospheric mantle to circular patterns in the asthenosphere. The high-V Isabella anomaly beneath the Great Valley is better interpreted as a remnant of the fossil Farallon slab currently experiencing a possible process of lithospheric downwelling based on the resulting negative radial anisotropy and coherent N-S fast orientations of azimuthal anisotropy in its lithosphere. The downwelling of the Isabella anomaly in turn may induce mantle upwelling, which is twisted by the relative motion between the Pacific and North American plates along the SAF to flow horizontally when reaching the lower lithosphere. Such a flow system possibly contributes to the lithospheric delamination beneath areas surrounding the Great Valley where the delaminated lithospheric segments are clearly revealed as high-V anomalies at a depth of  $>300$  km. Rifting developments beneath the Inner Borderland and the Salton Trough are revealed to have close associations with regional mantle upwelling and the relative motion between the Pacific and North American plates, respectively, based on the resulting distinct features of radial and azimuthal anisotropies.

#### Acknowledgments

Local and teleseismic travel time data are publicly available and downloaded from the Southern California Earthquake Data Center (<http://scedc.caltech.edu>) and the International Seismological Centre (<http://www.isc.ac.uk>), respectively. Thoughtful review comments and suggestions from Donald Forsyth, an anonymous referee, and Martha Savage (the Editor) significantly improved the manuscript. We thank Jianke Fan for thoughtful discussions. Codes from Stephen Gao and Kelly Liu are used to conduct two-layer fitting of SWS measurements. This work has been supported by the National Natural Science Foundation of China (grant 41606043) and the National Program on Global Change and Air-Sea Interaction (grant GASI-GEOGE-05) to Y. Yu, and Ministry of Education, Culture, Sports, Science and Technology (MEXT grant 26106005) to D. Zhao.

#### References

- Argus, D. F., Gordon, R. G., & DeMets, C. (2011). Geologically current motion of 56 plates relative to the no-net-rotation reference frame. *Geochemistry, Geophysics, Geosystems*, 12, Q11001. <https://doi.org/10.1029/2011GC003751>
- Atwater, T. (1970). Implications of plate tectonics for the Cenozoic tectonic evolution of western North America. *Geological Society of America Bulletin*, 81(12), 3513–3536. [https://doi.org/10.1130/0016-7606\(1970\)81\[3513:IOPTFT\]2.0.CO;2](https://doi.org/10.1130/0016-7606(1970)81[3513:IOPTFT]2.0.CO;2)
- Backus, G. E. (1965). Possible forms of seismic anisotropy of the uppermost mantle under oceans. *Journal of Geophysical Research*, 70(14), 3429–3439. <https://doi.org/10.1029/JZ070i014p03429>
- Barak, S., & Klemperer, S. L. (2016). Rapid variation in upper-mantle rheology across the San Andreas fault system and Salton trough, southernmost California, USA. *Geology*, 44(7), 575–578. <https://doi.org/10.1130/g37847.1>
- Beall, A. P., Moresi, L., & Stern, T. (2017). Dripping or delamination? A range of mechanisms for removing the lower crust or lithosphere. *Geophysical Journal International*, 210(2), 671–692. <https://doi.org/10.1093/gji/ggx202>
- Bird, P., & Rosenstock, R. W. (1984). Kinematics of present crust and mantle flow in southern California. *Geological Society of America Bulletin*, 95(8), 946–957. [https://doi.org/10.1130/0016-7606\(1984\)95<946:KOPCAM>2.0.CO;2](https://doi.org/10.1130/0016-7606(1984)95<946:KOPCAM>2.0.CO;2)
- Bonnin, M., Barruol, G., & Bokelmann, G. H. (2010). Upper mantle deformation beneath the North American–Pacific plate boundary in California from SKS splitting. *Journal of Geophysical Research*, 115, B04306. <https://doi.org/10.1029/2009JB006438>
- Boyd, O. S., Jones, C. H., & Sheehan, A. F. (2004). Foundering lithosphere imaged beneath the southern Sierra Nevada, California, USA. *Science*, 305(5684), 660–662. <https://doi.org/10.1126/science.1099181>

- Brothers, D. S., Driscoll, N. W., Kent, G. M., Harding, A. J., Babcock, J. M., & Baskin, R. L. (2009). Tectonic evolution of the Salton Sea inferred from seismic reflection data. *Nature Geoscience*, 2(8), 581–584. <https://doi.org/10.1038/ngeo590>
- Cox, P., Stubailo, I., & Davis, P. (2016). Receiver function and geometric tomography along the Monterey microplate to test slab delamination or lithospheric drip models of the Isabella anomaly, California. *Bulletin of the Seismological Society of America*, 106(1), 267–280. <https://doi.org/10.1785/0120140339>
- Elders, W. A., Rex, R. W., Robinson, P. T., Biehler, S., & Meidav, T. (1972). Crustal spreading in Southern California: The Imperial Valley and the Gulf of California formed by the rifting apart of a continental plate. *Science*, 178(4056), 15–24. <https://doi.org/10.1126/science.178.4056.15>
- Fay, N. P., Bennett, R. A., Spinler, J. C., & Humphreys, E. D. (2008). Small-scale upper mantle convection and crustal dynamics in Southern California. *Geochemistry, Geophysics, Geosystems*, 9, Q08006. <https://doi.org/10.1029/2008GC001988>
- Gao, S., Davis, P. M., Liu, H., Slack, P. D., Rigor, A. W., Zorin, Y. A., et al. (1997). SKS splitting beneath continental rift zones. *Journal of Geophysical Research*, 102(B10), 22,781–22,797. <https://doi.org/10.1029/97JB01858>
- Gao, S. S., & Liu, K. H. (2009). Significant seismic anisotropy beneath the southern Lhasa terrane, Tibetan Plateau. *Geochemistry, Geophysics, Geosystems*, 10, Q02008. <https://doi.org/10.1029/2008GC002227>
- Gilbert, H., Yang, Y., Forsyth, D. W., Jones, C. H., Owens, T. J., Zandt, G., & Stachnik, J. C. (2012). Imaging lithospheric foundering in the structure of the Sierra Nevada. *Geosphere*, 8(6), 1310–1330. <https://doi.org/10.1130/GES00790.1>
- Göögüs, O. H., Pusklywec, R. N., Şengör, A. M. C., & Gün, E. (2017). Drip tectonics and the enigmatic uplift of the Central Anatolian Plateau. *Nature Communications*, 8(1), 1538. <https://doi.org/10.1038/s41467-017-01611-3>
- Han, L., Hole, J. A., Stock, J. M., Fuis, G. S., Kell, A., Driscoll, N. W., et al. (2016). Continental rupture and the creation of new crust in the Salton trough rift, Southern California and northern Mexico: Results from the Salton Seismic Imaging Project. *Journal of Geophysical Research: Solid Earth*, 121, 7469–7489. <https://doi.org/10.1002/2016JB013139>
- Hartog, R., & Schwartz, S. Y. (2001). Depth-dependent mantle anisotropy below the San Andreas Fault system: Apparent splitting parameters and waveforms. *Journal of Geophysical Research*, 106(B3), 4155–4167. <https://doi.org/10.1029/2000JB900382>
- Hauksson, E. (2000). Crustal structure and seismicity distribution adjacent to the Pacific and North America plate boundary in southern California. *Journal of Geophysical Research*, 105(B6), 13,875–13,903. <https://doi.org/10.1029/2000JB900016>
- Houseman, G. A., & Molnar, P. (1997). Gravitational (Rayleigh-Taylor) instability of a layer with non-linear viscosity and convective thinning of continental lithosphere. *Geophysical Journal International*, 128(1), 125–150. <https://doi.org/10.1111/j.1365-246X.1997.tb04075.x>
- Huang, Z., & Zhao, D. (2013). Mapping P-wave azimuthal anisotropy in the crust and upper mantle beneath the United States. *Physics of the Earth and Planetary Interiors*, 225, 28–40. <https://doi.org/10.1016/j.pepi.2013.10.003>
- Huang, Z., Zhao, D., & Liu, X. (2015). On the trade-off between seismic anisotropy and heterogeneity: Numerical simulations and application to Northeast Japan. *Journal of Geophysical Research: Solid Earth*, 120, 3255–3277. <https://doi.org/10.1002/2014JB011784>
- Humphreys, E., Clayton, R. W., & Hager, B. H. (1984). A tomographic image of mantle structure beneath southern California. *Geophysical Research Letters*, 11(7), 625–627. <https://doi.org/10.1029/GL011i007p00625>
- Humphreys, E. D., & Hager, B. H. (1990). A kinematic model for the late Cenozoic development of southern California crust and upper mantle. *Journal of Geophysical Research*, 95(B12), 19,747–19,762. <https://doi.org/10.1029/JB095iB12p19747>
- Jiang, C., Schmandt, B., Hansen, S. M., Dougherty, S. L., Clayton, R. W., Farrell, J., & Lin, F. C. (2018). Rayleigh and S wave tomography constraints on subduction termination and lithospheric foundering in central California. *Earth and Planetary Science Letters*, 488, 14–26. <https://doi.org/10.1016/j.epsl.2018.02.009>
- Jones, C. H., Reeg, H., Zandt, G., Gilbert, H., Owens, T. J., & Stachnik, J. (2014). P-wave tomography of potential convective downwellings and their source regions, Sierra Nevada, California. *Geosphere*, 10(3), 505–533. <https://doi.org/10.1130/GES00961.1>
- Kosarian, M., Davis, P. M., Tanimoto, T., & Clayton, R. W. (2011). The relationship between upper mantle anisotropic structures beneath California, transpression, and absolute plate motions. *Journal of Geophysical Research*, 116, B08307. <https://doi.org/10.1029/2010JB007742>
- Lachenbruch, A. H., & Sass, J. H. (1980). Heat flow and energetics of the San Andreas fault zone. *Journal of Geophysical Research*, 85(B11), 6185–6222. <https://doi.org/10.1029/JB085iB11p06185>
- Lachenbruch, A. H., Sass, J. H., & Galanis, S. P. (1985). Heat flow in southernmost California and the origin of the Salton Trough. *Journal of Geophysical Research*, 90(B8), 6709–6736. <https://doi.org/10.1029/JB090iB08p06709>
- Lee, E. J., Chen, P., Jordan, T. H., Maechling, P. B., Denolle, M. A., & Beroza, G. C. (2014). Full-3-D tomography for crustal structure in southern California based on the scattering-integral and the adjoint-wavefield methods. *Journal of Geophysical Research: Solid Earth*, 119, 6421–6451. <https://doi.org/10.1002/2014JB011346>
- Lekic, V., French, S. W., & Fischer, K. M. (2011). Lithospheric thinning beneath rifted regions of southern California. *Science*, 334(6057), 783–787. <https://doi.org/10.1126/science.1208898>
- Lewis, J. L., Day, S. M., Magistrale, H., Eakins, J., & Vernon, F. (2000). Regional crustal thickness variations of the Peninsular Ranges, southern California. *Geology*, 28(4), 303–306. [https://doi.org/10.1130/0091-7613\(2000\)28<303:RCTVOT>2.0.CO;2](https://doi.org/10.1130/0091-7613(2000)28<303:RCTVOT>2.0.CO;2)
- Li, A., Dave, R., & Yao, Y. (2017). Crust and mantle deformation revealed from high-resolution radially anisotropic velocity models. In AGU Fall Meeting Abstracts.
- Li, Z., & Peng, Z. (2017). Stress-and structure-induced anisotropy in southern California from two decades of shear wave splitting measurements. *Geophysical Research Letters*, 44, 9607–9614. <https://doi.org/10.1002/2017GL075163>
- Lin, F. C., Ritzwoller, M. H., Yang, Y., Moschetti, M. P., & Fouch, M. J. (2011). Complex and variable crustal and uppermost mantle seismic anisotropy in the western United States. *Nature Geoscience*, 4(1), 55–61. <https://doi.org/10.1038/ngeo1036>
- Lin, Y. P., Zhao, L., & Hung, S. H. (2014). Full-wave multiscale anisotropy tomography in Southern California. *Geophysical Research Letters*, 41, 8809–8817. <https://doi.org/10.1002/2014GL061855>
- Liu, H., Davis, P. M., & Gao, S. (1995). SKS splitting beneath southern California. *Geophysical Research Letters*, 22(7), 767–770. <https://doi.org/10.1029/95GL00487>
- Liu, X., & Zhao, D. (2017). Depth-varying azimuthal anisotropy in the Tohoku subduction channel. *Earth and Planetary Science Letters*, 473, 33–43. <https://doi.org/10.1016/j.epsl.2017.05.034>
- Long, M. D., & Silver, P. G. (2008). The subduction zone flow field from seismic anisotropy: A global view. *Science*, 319(5861), 315–318. <https://doi.org/10.1126/science.1150809>
- Manley, C. R., Glazner, A. F., & Farmer, G. L. (2000). Timing of volcanism in the Sierra Nevada of California: Evidence for Pliocene delamination of the batholithic root? *Geology*, 28(9), 811–814. [https://doi.org/10.1130/0091-7613\(2000\)28<811:TOVITS>2.0.CO;2](https://doi.org/10.1130/0091-7613(2000)28<811:TOVITS>2.0.CO;2)
- Marone, F., & Romanowicz, B. (2007). The depth distribution of azimuthal anisotropy in the continental upper mantle. *Nature*, 447(7141), 198–201. <https://doi.org/10.1038/nature05742>
- Maupin, V., & Park, J. (2007). Theory and observations-wave propagation in anisotropic media. In G. Schubert (Ed.), *Seismology and the Structure of the Earth, Treatise on Geophysics* (Vol. 1, pp. 289–321). New York: Elsevier.

- Meade, B. J., & Hager, B. H. (2005). Block models of crustal motion in southern California constrained by GPS measurements. *Journal of Geophysical Research*, 110, B03403. <https://doi.org/10.1029/2004JB003209>
- Molnar, P., & Dayem, K. E. (2010). Major intracontinental strike-slip faults and contrasts in lithospheric strength. *Geosphere*, 6(4), 444–467. <https://doi.org/10.1130/GES00519.1>
- Montagner, J. P., Griot-Pommere, D. A., & Lavé, J. (2000). How to relate body wave and surface wave anisotropy? *Journal of Geophysical Research*, 105(B8), 19,015–19,027. <https://doi.org/10.1029/2000JB900015>
- Monteiller, V., & Chevrot, S. (2011). High-resolution imaging of the deep anisotropic structure of the San Andreas Fault system beneath southern California. *Geophysical Journal International*, 186(2), 418–446. <https://doi.org/10.1111/j.1365-246X.2011.05082.x>
- Nicholson, C., Sorlien, C. C., Atwater, T., Crowley, J. C., & Luyendyk, B. P. (1994). Microplate capture, rotation of the western Transverse Ranges, and initiation of the San Andreas transform as a low-angle fault system. *Geology*, 22(6), 491–495. [https://doi.org/10.1130/0091-7613\(1994\)022<0491:MCROTW>2.3.CO;2](https://doi.org/10.1130/0091-7613(1994)022<0491:MCROTW>2.3.CO;2)
- Özalaybey, S., & Savage, M. K. (1995). Shear-wave splitting beneath western United States in relation to plate tectonics. *Journal of Geophysical Research*, 100(B9), 18,135–18,149. <https://doi.org/10.1029/95JB00715>
- Pikser, J. E., Forsyth, D. W., & Hirth, G. (2012). Along-strike translation of a fossil slab. *Earth and Planetary Science Letters*, 331, 315–321.
- Polet, J., & Kanamori, H. (2002). Anisotropy beneath California: Shear wave splitting measurements using a dense broadband array. *Geophysical Journal International*, 149(2), 313–327. <https://doi.org/10.1046/j.1365-246X.2002.01630.x>
- Porter, R., Zandt, G., & McQuarrie, N. (2011). Pervasive lower-crustal seismic anisotropy in Southern California: Evidence for underplated schists and active tectonics. *Lithosphere*, 3(3), 201–220. <https://doi.org/10.1130/L126.1>
- Raikes, S. A. (1980). Regional variations in upper mantle structure beneath southern California. *Geophysical Journal International*, 63(1), 187–216. <https://doi.org/10.1111/j.1365-246X.1980.tb02616.x>
- Ramsay, J., Kohler, M. D., Davis, P. M., Wang, X., Holt, W., & Weeraratne, D. S. (2016). Anisotropy from SKS splitting across the Pacific-North America plate boundary offshore southern California. *Geophysical Journal International*, 207(1), 244–258. <https://doi.org/10.1093/gji/ggw27>
- Reeves, Z., Lekić, V., Schmerr, N., Kohler, M., & Weeraratne, D. (2015). Lithospheric structure across the California Continental Borderland from receiver functions. *Geochemistry, Geophysics, Geosystems*, 16, 246–266. <https://doi.org/10.1002/2014GC005617>
- Savage, M. K. (1999). Seismic anisotropy and mantle deformation: What have we learned from shear wave splitting? *Reviews of Geophysics*, 37(1), 65–106. <https://doi.org/10.1029/98RG02075>
- Savage, M. K., & Silver, P. G. (1993). Mantle deformation and tectonics: Constraints from seismic anisotropy in the western United States. *Physics of the Earth and Planetary Interiors*, 78(3–4), 207–227. [https://doi.org/10.1016/0031-9201\(93\)90156-4](https://doi.org/10.1016/0031-9201(93)90156-4)
- Schmandt, B., & Humphreys, E. (2010). Seismic heterogeneity and small-scale convection in the southern California upper mantle. *Geochemistry, Geophysics, Geosystems*, 11, Q05004. <https://doi.org/10.1029/2010GC003042>
- Sigloch, K., McQuarrie, N., & Nolet, G. (2008). Two-stage subduction history under North America inferred from multiple-frequency tomography. *Nature Geoscience*, 1(7), 458–462. <https://doi.org/10.1038/ngeo231>
- Silver, P. G., & Chan, W. W. (1991). Shear wave splitting and subcontinental mantle deformation. *Journal of Geophysical Research*, 96(B10), 16,429–16,454. <https://doi.org/10.1029/91JB00899>
- Silver, P. G., & Holt, W. E. (2002). The mantle flow field beneath western North America. *Science*, 295(5557), 1054–1057. <https://doi.org/10.1126/science.1066878>
- Silver, P. G., & Savage, M. K. (1994). The interpretation of shear-wave splitting parameters in the presence of two anisotropic layers. *Geophysical Journal International*, 119(3), 949–963. <https://doi.org/10.1111/j.1365-246X.1994.tb04027.x>
- Tanimoto, T., & Prindle Sheldrake, K. (2002). Three-dimensional S-wave velocity structure in southern California. *Geophysical Research Letters*, 29(8), 1223. <https://doi.org/10.1029/2001GL013486>
- Tape, C., Liu, Q., Maggi, A., & Tromp, J. (2009). Adjoint tomography of the southern California crust. *Science*, 325(5943), 988–992. <https://doi.org/10.1126/science.1175298>
- Tape, C., Plesch, A., Shaw, J. H., & Gilbert, H. (2012). Estimating a continuous Moho surface for the California unified velocity model. *Seismological Research Letters*, 83(4), 728–735. <https://doi.org/10.1785/022011018>
- Tian, Y., Zhao, D., & Teng, J. (2007). Deep structure of southern California. *Physics of the Earth and Planetary Interiors*, 165(1–2), 93–113. <https://doi.org/10.1016/j.pepi.2007.08.003>
- Wang, J., & Zhao, D. (2008). P-wave anisotropic tomography beneath Northeast Japan. *Physics of the Earth and Planetary Interiors*, 170(1–2), 115–133. <https://doi.org/10.1016/j.pepi.2008.07.042>
- Wang, J., & Zhao, D. (2013). P-wave tomography for 3-D radial and azimuthal anisotropy of Tohoku and Kyushu subduction zones. *Geophysical Journal International*, 193(3), 1166–1181. <https://doi.org/10.1093/gji/ggt086>
- Wang, Y., Forsyth, D. W., Rau, C. J., Carrero, N., Schmandt, B., Gaherty, J. B., & Savage, B. (2013). Fossil slabs attached to unsubducted fragments of the Farallon plate. *Proceedings of the National Academy of Sciences*, 110(14), 5342–5346. <https://doi.org/10.1073/pnas.1214880110>
- Wei, W., Zhao, D., Xu, J., Zhou, B., & Shi, Y. (2016). Depth variations of P-wave azimuthal anisotropy beneath Mainland China. *Scientific Reports*, 6(1), 29614. <https://doi.org/10.1038/srep29614>
- West, J. D., Fouch, M. J., Roth, J. B., & Elkins-Tanton, L. T. (2009). Vertical mantle flow associated with a lithospheric drip beneath the Great Basin. *Nature Geoscience*, 2(6), 439–444. <https://doi.org/10.1038/ngeos526>
- Yang, B. B., Liu, K. H., Dahm, H. H., & Gao, S. (2016). A uniform database of teleseismic shear-wave splitting measurements for the western and central United States: December 2014 update. *Seismological Research Letters*, 87(2A), 295–300. <https://doi.org/10.1785/0220150213>
- Yang, Y., & Forsyth, D. W. (2006). Rayleigh wave phase velocities, small-scale convection, and azimuthal anisotropy beneath southern California. *Journal of Geophysical Research*, 111, B07306. <https://doi.org/10.1029/2005JB004180>
- Yu, Y., Liu, K. H., Huang, Z., Zhao, D., Reed, C. A., Moidaki, M., & Gao, S. S. (2017). Mantle structure beneath the incipient Okavango rift zone in southern Africa. *Geosphere*, 13(1), 102–111. <https://doi.org/10.1130/GES01331.1>
- Zandt, G., Gilbert, H., Owens, T. J., Dueca, M., Saleeby, J., & Jones, C. H. (2004). Active foundering of a continental arc root beneath the southern Sierra Nevada in California. *Nature*, 431(7004), 41–46. <https://doi.org/10.1038/nature02847>
- Zandt, G., & Humphreys, E. (2008). Toroidal mantle flow through the western US slab window. *Geology*, 36(4), 295–298. <https://doi.org/10.1130/G24611A.1>
- Zhang, H., Zhao, D., Yu, C., & Zhao, J. (2016). Varying deformation patterns in central Tibet revealed by radial anisotropy tomography. *Journal of Geophysical Research: Solid Earth*, 121, 3445–3461. <https://doi.org/10.1002/2016JB012832>
- Zhang, S., & Karato, S. I. (1995). Lattice preferred orientation of olivine aggregates deformed in simple shear. *Nature*, 375(6534), 774–777. <https://doi.org/10.1038/375774a0>
- Zhao, D., Hasegawa, A., & Horiuchi, S. (1992). Tomographic imaging of P and S wave velocity structure beneath northeastern Japan. *Journal of Geophysical Research*, 97(B13), 19,909–19,928. <https://doi.org/10.1029/92JB00603>

- Zhao, D., Hasegawa, A., & Kanamori, H. (1994). Deep structure of Japan subduction zone as derived from local, regional, and teleseismic events. *Journal of Geophysical Research*, 99(B11), 22313–22329. <https://doi.org/10.1029/94JB01149>
- Zhao, D., Kanamori, H., & Humphreys, E. (1996). Simultaneous inversion of local and teleseismic data for the crust and mantle structure of southern California. *Physics of the Earth and Planetary Interiors*, 93(3–4), 191–214. [https://doi.org/10.1016/0031-9201\(95\)03076-X](https://doi.org/10.1016/0031-9201(95)03076-X)
- Zhao, D., Yu, S., & Liu, X. (2016). Seismic anisotropy tomography: New insight into subduction dynamics. *Gondwana Research*, 33, 24–43. <https://doi.org/10.1016/j.gr.2015.05.008>